



Adjustable Injection Currents: The Benefits of Controllable Inductors in Current Injection HVDC Circuit Breakers

Other Publication

Author(s):

[Schultz, Tim](#) ; [Spren, L. Brook](#); [Franck, Christian](#) 

Publication date:

2020-02-19

Permanent link:

<https://doi.org/10.3929/ethz-b-000400308>

Rights / license:

[Creative Commons Attribution-NonCommercial-ShareAlike 4.0 International](#)

Adjustable Injection Currents: The Benefits of Controllable Inductors in Current Injection HVDC Circuit Breakers

T. Schultz, L. B. Spreen, C. M. Franck

High Voltage Laboratory, ETH Zurich, Physikstrasse 3, 8092, Zurich, Switzerland
cfranck@ethz.ch

Abstract:

Economic and robust high voltage direct current (HVDC) circuit breakers are a strategic technology in the development of next-generation power transmission. Current injection circuit breakers require fewer complex components than other technologies, making them economically attractive. The limiting factor, however, remains the high current and voltage gradients which occur at zero current during the interruption of low fault currents.

This paper investigates a novel current injection topology that generates adjustable injection currents. This is realized by controlling the injection circuit inductance via a non-linear magnetic core. The inductance varies according to the core's saturation state, which is manipulated by at least one control winding carrying a quasi-DC current. By holding inductance low at the beginning of injection, a minimal time-to-interruption may be achieved. Increasing inductance shortly before interruption reduces both the current gradient and ensuing transient voltages, thus reducing stresses on the mechanical interrupter.

In this paper, a simulation model for the proposed controllable inductor is developed and compared to results of a scaled-down experiment. On this basis, the topology is dimensioned for the use in a 320 kV network. The conducted simulations illustrate both feasibility and advantages of the novel topology compared to a reference current injection circuit.

Keywords: HVDC Circuit Breaker Topologies, Mechanical Circuit Breaker, Current Injection, Controllable Inductor, Magnetic Amplifier

1 Introduction

The exploitation of decentralized local and centralized but remote renewable energy sources has considerably influenced the structure of power generation in recent years. This has led to changing requirements in energy transmission and sparked a new wave of research in HVDC technology.

In addition to a growing number of HVDC point-to-point connections, the first multiterminal HVDC grids have been implemented [1–3]. As in HVAC, meshed grids require protection systems, including circuit breakers, that can interrupt fault currents and isolate faulty components from the grid. However, the requirements for fault current interruption in HVDC grids differs from HVAC. The most notable difference is the absence of a natural current zero crossing, which renders mechanical interrupters (MI), which are used in HVAC, ineffective. Additionally, faster fault clearance is required. [4]

To meet the requirements for fault current interruption in HVDC networks, a large number of different circuit breaker topologies have been proposed [5–7]. The general structure is typically composed of three branches, the nominal current path (NCP), the current commutation path (CCP) and the energy absorption path (EAP). The NCP is optimized for low resistance and carries the current if the circuit breaker is in closed state. It consists of a mechanical switch, which is either an ultra-fast disconnecter or a mechanical interrupter. For current interruption, the current can be commutated into the CCP and the mechanical switch can be opened. Afterwards, a counter voltage is built up in the CCP. In the final step, the current is commutated into a surge arrester (SA) in the EAP, which limits the overvoltage to its clamping voltage and brings the fault current to leakage current level.

One promising DC circuit breaker realization is the current injection topology (cf. Figure 1). It consists of a mechanical interrupter (MI) in the NCP and a combination of pre-charged capacitor (C_{INJ}), inductor (L_{INJ}) and injection switch (S_{INJ}) in the CCP. When a fault is detected, the MI is signalled to open, drawing an arc, when a fault occurs. As soon as the contact distance of the MI is sufficient to withstand the transient interruption voltage (TIV), the injection switch is closed and a counter current is injected into the NCP to create an artificial current zero crossing. If the MI interrupts the fault

current in the NCP, the current flow is diverted into the CCP, charging up the injection capacitor. The fault current starts to decrease as soon as the grid voltage is exceeded. When the clamping voltage of the SA is reached, the current commutates into the EAP, where excess energy is dissipated.

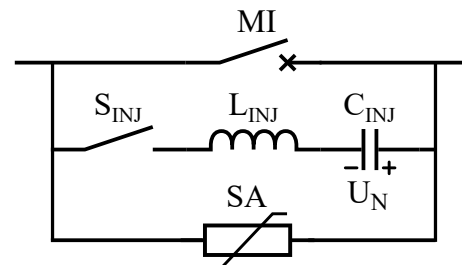


Fig. 1: Schematic drawing of the current injection topology

The current injection topology does not require expensive stacks of (fully controllable) semiconductors. The injection switch can be realized with a spark gap [8]. This creates an economic advantage over other topologies and makes the current injection topology a promising candidate for the use in HVDC grids.

The reference current injection topology provides a sinusoidal injection current with fixed amplitude. This leads to increasing stresses when interrupting lower fault currents, as the gradient at zero crossing is higher. The maximum gradient that can occur at zero crossing is defined by the injection inductance and the capacitor pre-charging voltage. In addition, the remaining voltage in the injection capacitor is higher for lower fault currents, leading to an increased rate of rise of the initial transient interruption voltage (ITIV). The interruption limits of the mechanical interrupter consequently define a lower limit for the dimensioning of the injection circuit capacitor and inductor.

Regarding the technology of the mechanical interrupter, gas [9, 10] and vacuum interrupters [11–13] as well as a series connection of both [14, 15] have been suggested. Vacuum interrupters offer higher current interruption limits, but a lower voltage withstand capability

than gas interrupters. A series connection is therefore required for high voltages, increasing system complexity.

Research on current injection topologies dates back to the early stages of HVDC circuit breaker research [11, 12]. While more complex topologies have been proposed in the recent years, current injection topologies still provide a promising option due to their economic advantages. This is mirrored in current research and the installation of current injection circuit breakers in one of the first HVDC grids [16–18].

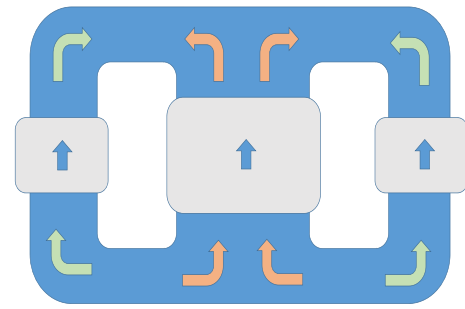
The commissioned current injection circuit breakers are based on a fixed injection current and a series connection of vacuum circuit breakers. However, current research suggests that interruption performance of current injection circuit breakers can be improved if a phase of decreased current gradient shortly before current zero crossing in the MI is added [19]. Such a phase can be generated by auxiliary circuits [20, 21]. The presented paper follows this line of thought with the introduction of an actively controllable inductor in the current injection circuit. This novel concept is derived from magnetic amplifiers and allows an active control of the inductance and thus shape of the injection current. It enables both a fast current zero creation and low stresses at interruption. This is possible by reducing the inductance of the injection circuit during the ramp-up phase of the injection current. The inductance is then increased shortly before the injection current creates the current zero crossing in the MI. This reduces both rate of rise of current (ROROC) before and rate of rise of voltage (ROROV) after current zero. In this paper, both simulations and measurements for a scaled down injection circuit have been conducted. Based on these, the simulation model is scaled to HVDC to illustrate the impact of the controllable inductor and investigate the feasibility of the concept. The results show that controllable inductors offer a promising solution to reduce capacitance and inductance in the injection circuit, further improving the economical advantage of the current injection topology. Additionally, controllable inductors can enable the use of a single gas interrupter instead of a stack of vacuum interrupters, due to the lowered interruption stresses. This further simplifies the topology.

2 Controllable inductors

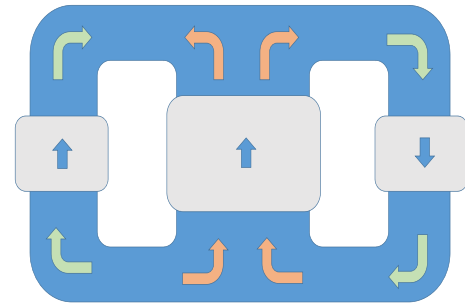
Controllable inductors (ContInd) consist of a main winding and a control winding that are linked by non-linear magnetic cores. The purpose of the control winding and its connected circuit is to set the working point of the core for the main winding by applying a DC or modulated current. The control circuit current can saturate or de-saturate the core, influencing the inductance seen by the main circuit. [22, 23]

Based on this operation principle, the controllable inductor can be used as a binary switch (saturated / non-saturated) or as a modulator, as evidenced by its use in transatlantic radio communication in the beginning of the 20th century [24]. A standard design of a controllable inductor uses E-cores with the main winding on the central and split control windings on the outer legs. Depending on the connection of the control windings, two configurations can be realized. Either the control windings are connected to create opposing fluxes (*trans*-configuration, Figure 2a) or fluxes in the same direction (*cis*-configuration, Figure 2b)

In the *cis*-configuration, the application of a DC bias on the control winding leads to a saturation of the outer parts of the core, in the central legs the fluxes compensate to a large extent. Consequently, the core is not completely saturated. If the main current is increased, it will create a flux that opposes the control flux in one leg and aligns with the flow direction in the other leg. This will drive one leg out of and one leg deeper into saturation. A further increase of main current will eventually lead to a saturation of all core legs as the flux generated by the main current starts to dominate. The *cis*-configuration allows a symmetrical operation, making it suitable for an operation with AC current on the main winding. The opposing connection of the control winding has the advantage that induced voltages from main winding current are equal but opposed, decoupling the effects from the control circuit.



(a) *trans* configuration



(b) *cis* configuration

Fig. 2: Controllable inductor on a three-legged core, outer: control windings, inner: main winding

In contrast, in the *trans*-configuration the control windings create opposing flows that also saturate the center leg of the core. A current in the main winding will cause a flux that either opposes both control fluxes or aligns with their direction. Thus, either driving the core out of saturation (and again into saturation with opposing flow direction for high main currents) or deeper into saturation. A symmetrical operation for the use of AC on the main winding is not possible. However, the *trans*-configuration offers the advantage of a larger unsaturated inductance of the main winding. As the control windings are not connected in opposed directions, voltages induced from the main into the auxiliary windings do not cancel each other.

In current injection circuit breaker topologies, the injection current is shaped by an LC circuit. As the inductance is fixed, the current is sinusoidal. A more favorable current shape would be reached if the initial inductance of the injection loop (NCP and CCP) would be low and increases before zero crossing in the MI to reduce ROROC. This can be achieved with a controllable inductor in the CCP. Shortly before current injection, the control circuit can be used to saturate the core, leading to a fast current increase at the beginning of the injection. If control and injection circuit are designed in such a way that the flux of the main winding de-saturates the core before zero crossing, the increased inductance of the NCP - CCP loop causes a decrease in ROROC and ROROV. The stresses for the MI during interruption thus can be decreased.

3 Simulation model

To help in the design process and for extrapolation to HVDC systems, a simulation model of the current injection topology with controllable inductor has been built. It is implemented using the PLECS® environment. The magnetic circuit is modelled with a saturable core and hysteresis is omitted. The magnetic field strength and the flux density are linked with an arctan fit, based on the following equation:

$$B = \frac{2}{\pi} B_{\text{sat}} \arctan\left(\frac{\pi H}{2a}\right) + \mu_0 H \quad (1)$$

$$a = \frac{B_{\text{sat}}}{\mu_{\text{non-sat}} - \mu_0} \quad (2)$$

Here, B_{sat} describes the saturation flux density, μ_0 the saturated (vacuum) permeability and $\mu_{\text{non-sat}}$ the unsaturated permeability. While this model does not account for hysteresis, it proved to be faster and more stable over the investigated parameter range.

4 Experimental setup

The test circuit for investigating the impact of a controllable inductor on the interruption performance of a current injection circuit breaker is depicted in Figure 3.

Fault currents are generated by a low frequency LC circuit that can be connected to the circuit breaker by a making switch (S_{FAU}). The investigated DC circuit breaker is based on the current injection scheme. A model gas interrupter serves as the mechanical switch in the NCP, using a fixed contact system with an ignition wire and compressed air for interruption [25].

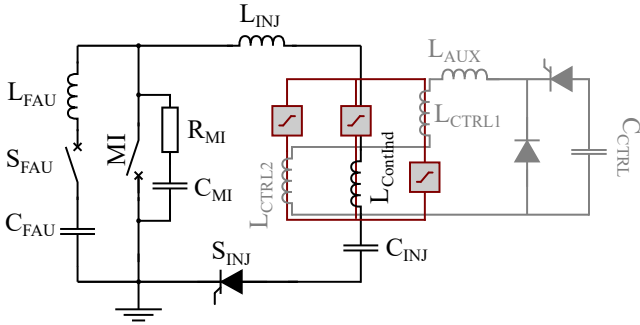


Fig. 3: Experimental setup for measuring interruption performance of current injection topologies, gray: control circuit, red: magnetic coupling

The inductance in the injection circuit consists of an air core inductor (L_{INJ}) and the controllable inductor (L_{ContInd}). The control circuit to apply a bias for core saturation consists of a pre-charged capacitor (C_{CTRL}), which can be discharged through a the control windings of the ContInd (L_{CTRL1} and L_{CTRL2}). A freewheeling diode ensures a unidirectional current flow.

In the freewheeling state, the current decays due to parasitic resistance of the circuit and diode losses. To increase the LR time constant and get closer to a quasi-DC current during the experiment, additional inductance is added (L_{aux}).

Table 1 Parameters of the test circuit

Component	Value	Component	Value
C_{FAU}	792 μF	C_{ctrl}	392 μF
L_{FAU}	7.5 mH	L_{aux}	125 μH
C_{INJ}	182 μF		
L_{INJ}	0.9 mH		

The controllable inductor is based on a double-E core design using two Micrometals E827-26 cores. The design parameters of the inductor are summarized in Table 2. A photo of the inductor used in the tests is shown in Figure 4. To maximize its effect and since only unidirectional current flow is required in the injection circuit, the controllable inductor is connected in *trans*-configuration.

Table 2 Parameters of the controllable inductor

Component	Value	Component	Value
A_m	41 cm^2	n_{main}	40
l_m	68 cm	n_{ctrl}	2 · 15
μ_r	75	B_{sat}	1.85 T

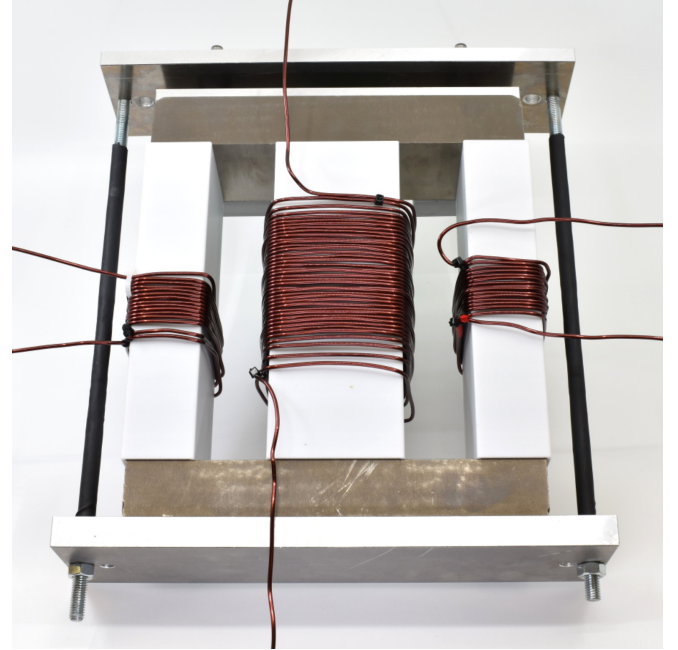


Fig. 4: Photo of the controllable inductor, the two E-cores are within a clamping system, control windings are on the outer legs, main winding on the inner, the core has a width of 21 cm and is isolated from the windings using white polycarbonate sleeves

To investigate the impact of the controllable inductor on the injection current, a series of measurements with fixed mechanical parameters and a variation of control circuit current (i.e. control circuit capacitor pre-charge) has been conducted.

Figure 5 shows an example of the measured control circuit current (i_{CTRL}), the voltage across one of the control circuit windings (u_{CTRL1}) as well as the current in the injection circuit (i_{INJ}). $t = 0$ s marks the start of the current injection. The control circuit is activated approximately 800 μs before current injection to ramp up the bias current. In the presented test, the pre-charge voltage of the control circuit is approximately 400 V and the peak current reaches slightly less than 1 kA.

The current injection (i_{INJ}) shows a slightly distorted wave shape due to the influence of the pre-saturated controllable inductor. It starts with a high current gradient, which after several tens of microseconds decreases as the flux generated by the main winding drives the core out of saturation. At a injection current level of approximately 400 A, the core is driven into saturation again, resulting in an increased current gradient ($t > 200 \mu\text{s}$).

A variation of the control circuit current by adjusting the pre-charge can shift the de-saturation region for the injection current to higher or lower currents. Figure 6 shows measured and simulated injection currents for a variation of the control circuit pre-charge from 0 V to 800 V. While both measurement and simulation show a shifting de-saturation region for a variation of control current, this effect is more pronounced in the simulation. Figure 7 shows the current gradient as a function of time for simulation and measurement. Here, the de-saturation region can be seen more clearly. For zero pre-charge, both simulation and measurement show a similar behavior. While both show the same general trends, the difference between simulation and measurement increases with increasing control current. The reduction in current gradient achieved in this example is approximately 40%.

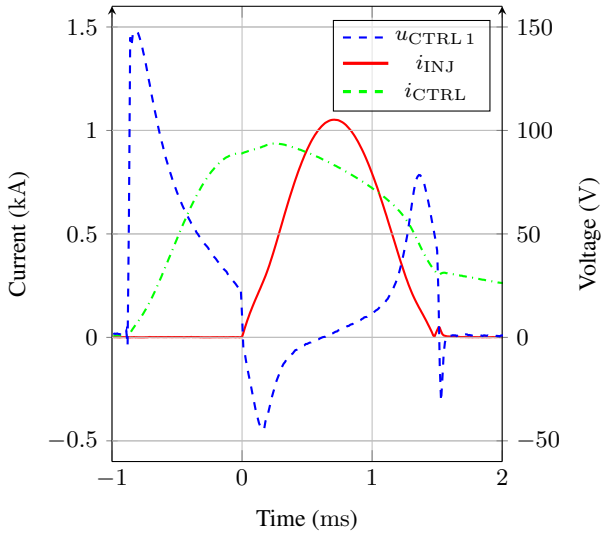


Fig. 5: Measured currents and voltages as function of time, control voltage $u_{CTRL}(t=0) = 400$ V

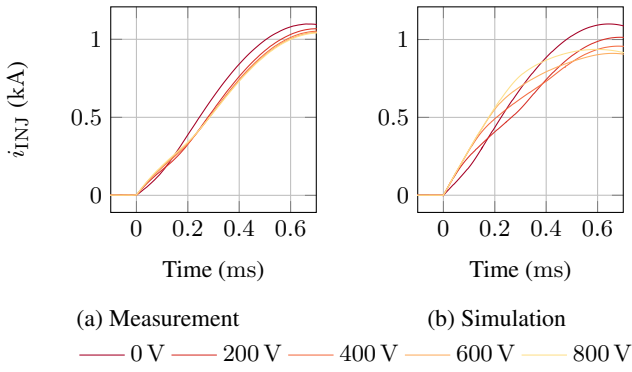


Fig. 6: Injection current as function of time for different control voltages $u_{CTRL}(t=0)$

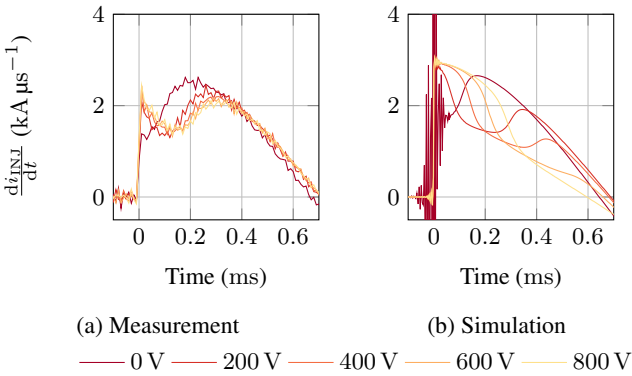


Fig. 7: $\frac{di_{INJ}}{dt}$ as function of time for different control voltages $u_{CTRL}(t=0)$

To complete the picture, the control current and the voltage across one of the two control windings are depicted in Figures 8 and 9 for both measurement and simulation. The control circuit current shows a similar time to peak, indicating that the L to C ratio is similar for simulation and experiment. In the simulation, peak current is higher, which can likely be attributed to a difference in damping due to skin effect and magnetization losses. Furthermore, differences in the real and simulated magnetization characteristic may influence the result.

A comparison of the control circuit currents after start of the injection current ($t > 0$ s) also indicates that the inductive coupling in the experiments is weaker than in the simulation. This difference can likely be related to geometry (fringing flux, non-homogeneous flux distribution in the core). While operating points for the core are also different due to the higher control current in the simulation, this should rather counteract the effect than pronounce it.

The control voltage also shows differences in absolute values but similarities in general trends. The initial voltage is higher for the simulation, which is probably due to the absence of parasitic capacitance between the turns of the windings. The induced voltage from the injection current is also higher in the simulation. Besides parasitic capacitance, this could also in part result from non-ideal linkage of the windings (e.g. fringing flux).

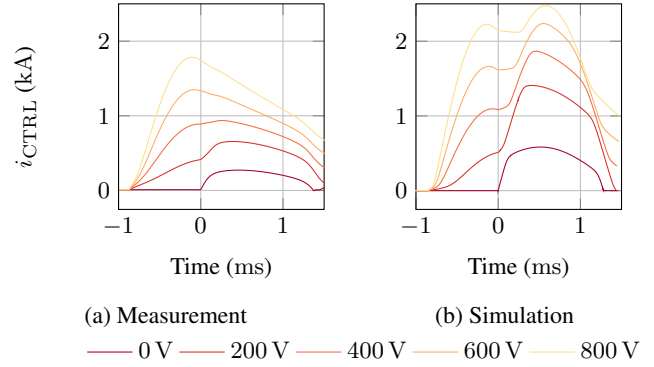


Fig. 8: Control circuit current for different control circuit voltages for different control voltages $u_{CTRL}(t=0)$

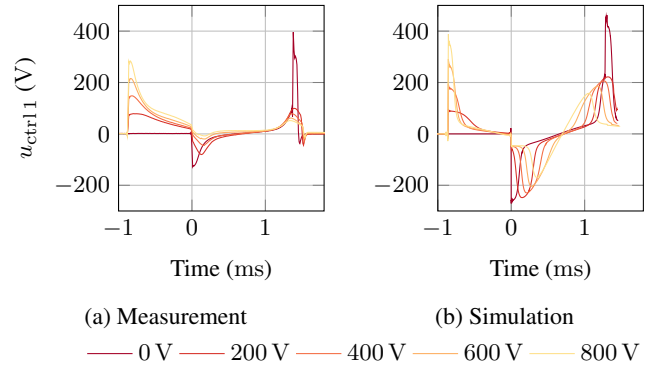


Fig. 9: Voltage across one of the two control circuit windings for different control voltages $u_{CTRL}(t=0)$

While the presented results show differences between measurement and simulation, they nonetheless exhibit consistent and predictable trends. This underlines the general suitability of the controllable inductor to influence gradients in current injection circuit breakers.

To derive the optimum control strategy for a given fault current, the injection current gradient can be plotted as a function of the injection current produced with different control circuit settings (here pre-charging voltage) as illustrated in Figure 10. The system can then be programmed to set the control currents / pre-charge voltages that lead to the lowest current gradient for a given fault current. To achieve this, it is necessary to predict the fault current level and adjust the control current such that a low current gradient is created at the anticipated zero crossing. The latter could be realized by replacing the control circuit thyristor with a fully controllable semiconductor switch. This switch can disconnect C_{CTRL} during ramping up of the injection current and initiate freewheeling at the desired current below the maximum.

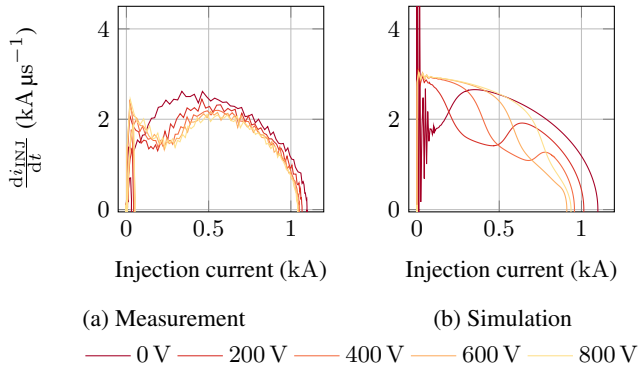


Fig. 10: Rate of rise of current as a function of injection current for different control voltages $u_{CTRL}(t=0)$

5 Controllable Inductors for HVDC Circuit Breakers

In this section, the feasibility to scale a controllable inductor for the use in HVDC circuit breakers is investigated. The characteristic values for the system are listed in Table 3. This table also includes data for a reference current injection topology for comparison with the design of the ContInd. A schematic of the simulated topology is depicted in Figure 11. To reduce the complexity, a two-legged design is chosen. For the control circuit, the same simple and robust design as in the experiments is used.

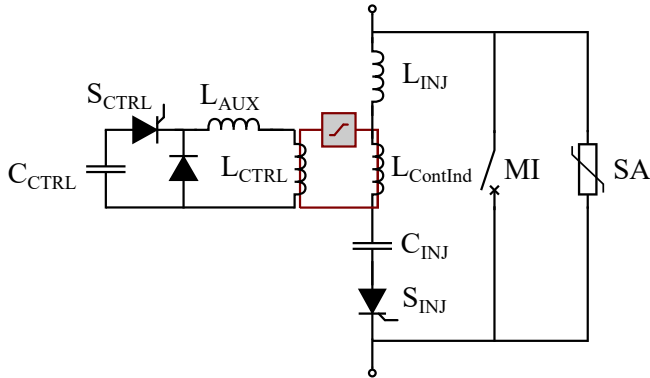


Fig. 11: Scaled setup for current injection circuit breaker with controllable inductor (two-legged design)

Table 3 System and component values for the reference topology (Ref) and a scaled ContInd topology

Component	Value	Component	Value
U_n	320 kV	ContInd	
I_0	2.0 kA	L_{INJ}	0 mH
L_{DC}	100 mH	C_{INJ}	1.2 μ F
R_{FAU}	0.1 Ω to 150 Ω		
Ref		Control circuit	
L_{INJ}	1.2 mH	C_{CTRL}	500 μ F
C_{INJ}	2 μ F	$U_{CTRL,0}$	0 kV to 25 kV
		L_{aux}	100 μ H

Figure 12 shows the interruption of a linear rising fault current for different control current levels. For zero control current, the de-saturation region with reduced current gradient is at low injection currents and thus at the beginning of the current injection. With increasing control current, the region can be shifted to higher injection currents and thus close to current zero crossing for the presented example. The width of the de-saturated region depends on current

gradient, geometry of the ContInd and the saturation flux density B_{sat} of the employed core material.

Table 4 ContInd dimensioning data, based on the material used in experimental investigations (Micrometals Mix-26)

Component	Value	Component	Value
n_{CTRL}	25	n_{main}	100
B_{sat}	1.85	A_m	246 cm ²
μ_r	75	l_{mag}	58 cm

The stresses on the control circuit are illustrated in Figures 13 and 14. The control current is ramped up approximately 2 ms before injection. For an improved detection of the fault current level that needs to be interrupted, this could also be delayed as the time to peak is only about 300 μ s. At $t=0$ s, the current injection starts and immediately influences the control current. This leads to higher stresses for the control circuit. However, the coupling is non-linear; as soon as the core is in saturation, the coupling is drastically reduced.

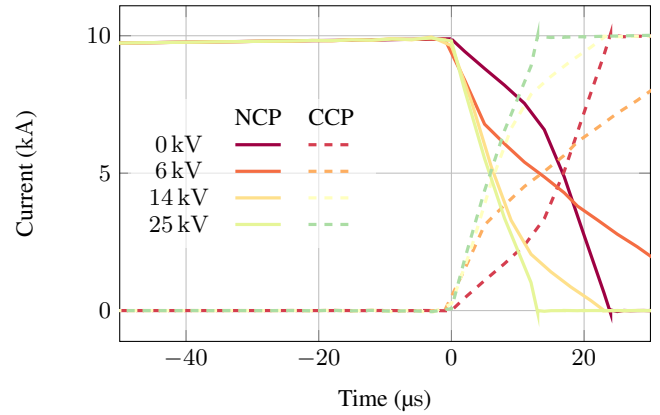


Fig. 12: NCP and CCP current of the ContInd topology as function of time for different control voltages for different pre-charging voltages of C_{CTRL} . In this case, $U_{CTRL,0} = 14$ kV produces a low current gradient at the zero crossing.

The voltages that stress the control windings are highest when injection is started. They do not exceed 80 kV, which defines the isolation requirements of the winding. For the semiconductor, the maximum charging voltage of the control circuit capacitor defines the voltage withstand requirement, as the circuit is in freewheeling for the rest of the operation.

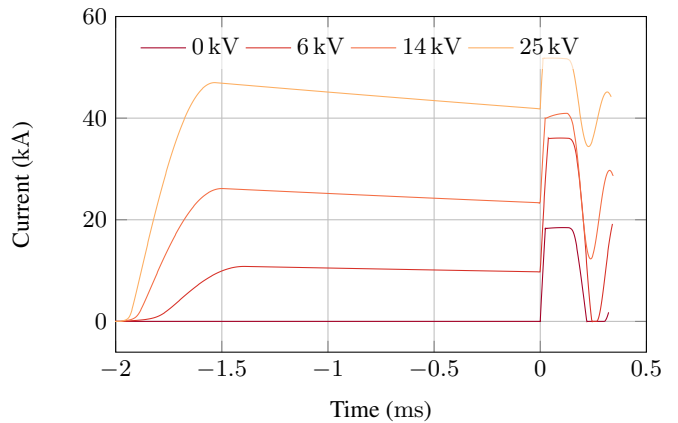


Fig. 13: ContInd control current as function of time for different pre-charging voltages of C_{CTRL}

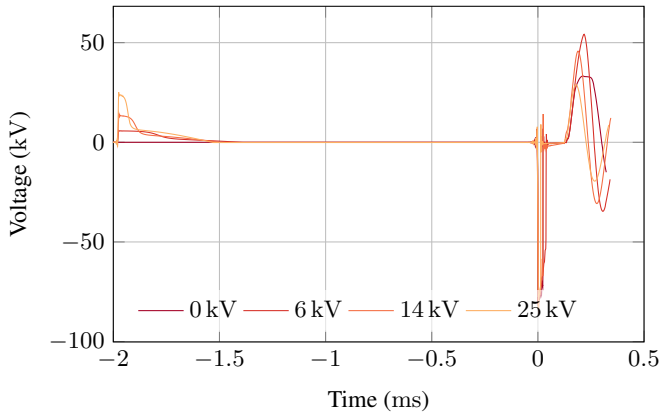


Fig. 14: Control winding (L_{CTRL}) voltage as a function of time for different pre-charging voltages of C_{CTRL}

Figures 15, 16 and 17 show current gradient, voltage gradient and ϵ , the product of both, as functions of fault and control current.

Voltage and current gradients show a similar behavior. If the de-saturated phase occurs at an injection current that is equal to the fault current, the injection circuit inductance is high when the current in the MI crosses zero. This leads to a low current gradient before zero crossing. After interruption, the remaining charge in the injection capacitor discharges into the MI's stray capacitance, causing the initial transient interruption voltage. This balancing of charges is limited by the inductance in NCP and CCP. As the controllable inductor is in a de-saturated state, the voltage gradient after zero crossing is reduced. The product of both current and voltage gradient (ϵ) can be used as a measure for the stresses the MI experiences during interruption. The figures show that by using the correct control current, ϵ can be reduced drastically.

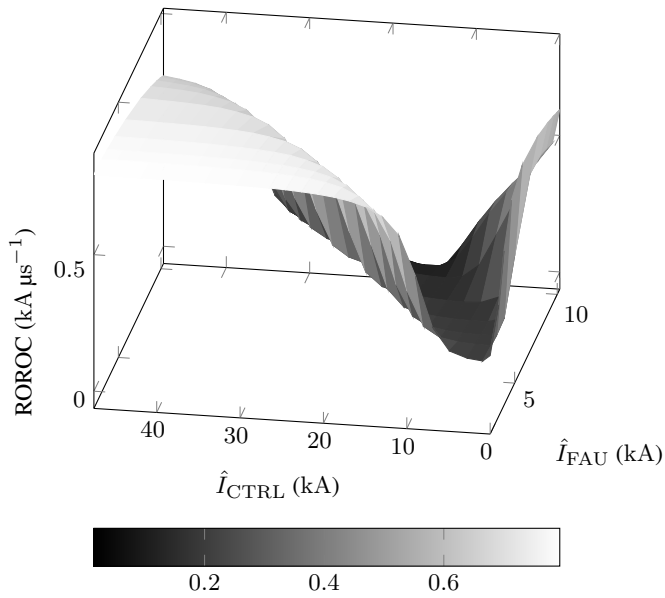


Fig. 15: Rate of rise of current as a function of fault and control current

Figure 17 illustrates that a control current in the range between almost zero and approximately 20 kA is sufficient to cover the complete range of tested fault currents. In the simulated configuration, this can be reached with a maximum charging voltage of approximately 11 kV. Consequently, a stack of two series connected devices for both diode and thyristor (S_{CTRL}) would be sufficient.

Regarding the control circuit, a simple design was chosen for simulation as its behavior before the freewheeling does not impact the

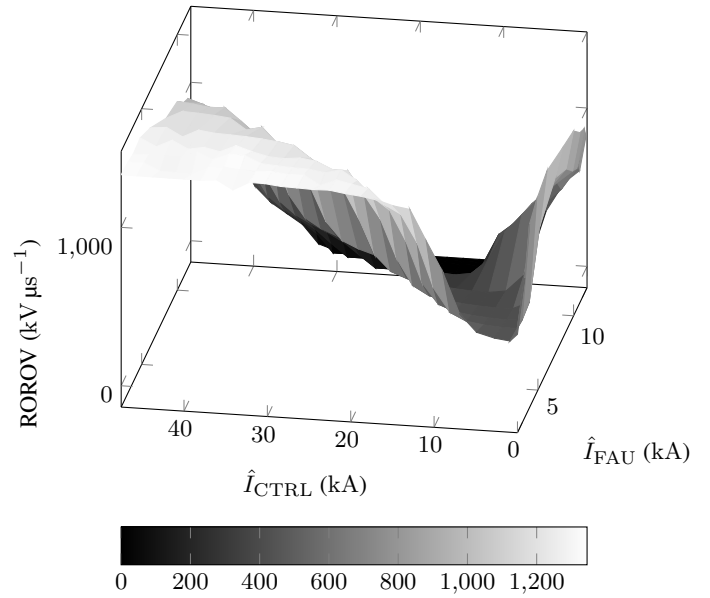


Fig. 16: Rate of rise of ITIV as a function of fault and control current

performance of the ContInd. To facilitate adjusting the control current to the required level, the illustrated design (cf. Figure 11) can be updated by using a fully controllable semiconductor switch (IGBT, IGCT) for S_{CTRL} . In this case, C_{CTRL} can always be charged to the maximum required voltage. To set the control current, S_{CTRL} only has to be turned off during the ramp-up of the control current when the required value is reached and force the control circuit into freewheeling.

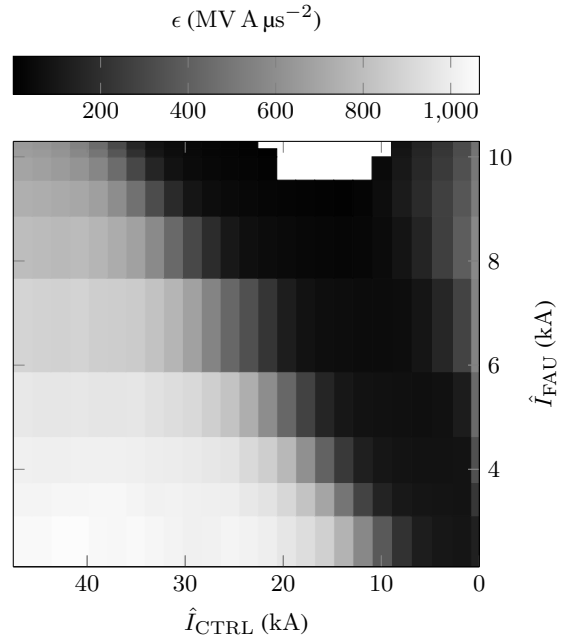


Fig. 17: ϵ as a function of fault and control current, no current zero crossings above approximately 9.5 kA for control currents between 10 kA and 20 kA

In Figure 18, the interruption stresses for the reference configuration (Ref) as well as the controllable inductor are illustrated. For the controllable inductor, examples are depicted for fixed control currents (orange, dotted). Selecting the optimum control current yields the lowest achievable stresses for the MI (orange, solid).

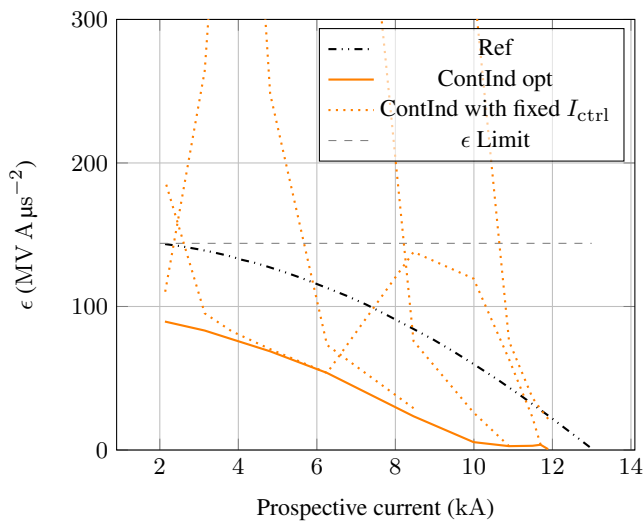


Fig. 18: Comparison of ϵ as a function of interrupted current for reference configuration and controllable inductor, dotted lines represent CI with fixed injection current

With the implemented design, the ContInd is able to fulfill the interruption requirements of the MI over the complete range investigated. Stresses for the MI are even lower than for Ref. Compared to the reference configuration, the injection circuit of the ContInd employs a smaller capacitor (60% capacitance at same voltage rating) and no linear inductor. The ContInd additionally requires energy storage to create the control current. In the presented dimensioning, the control circuit capacitor would be equivalent to approximately 11% of additional capacitance at the voltage rating of the injection capacitor based on the stored energy. The control circuit also contains a small linear inductor, but due to the lower inductance and voltage rating, it does not add significant cost. The required semiconductors add some cost. However, due to the moderate voltage rating of the control circuit, this is expected to be minor compared to the injection circuit. Still, an additional control system to determine fault current levels and adjust injection currents is required, which has not been investigated within this thesis. The different components make it difficult to tell if there is an overall cost advantage and how large this would be. However, the simulations clearly indicate that it is feasible to scale the proposed concept and obtain a better switching performance, which could even come at reduced cost.

6 Conclusion

The key element of current injection circuit breakers for HVDC are mechanical interrupters. Their interruption limits, i.e. rate of rise of current before and rate of rise of voltage after current zero crossing, set a lower boundary for the required capacitance and inductance in the injection circuit. This has a significant influence on the size and cost of the whole topology. Furthermore, the fixed injection currents lead to increasing stresses for interrupting low (fault) currents. Consequently, improving current injection waveforms is a promising way to improve the performance of current injection topologies.

In this paper, a novel current injection circuit breaker has been introduced. The injection circuit uses a controllable inductor to adaptively shape the injection current based on the fault current that must be interrupted. It is able to ramp up the injection current quickly and reach a fast current zero crossing by actively saturating the injection circuit inductor. Additionally, it can reduce rate of rise of current before and rate of rise of voltage after current zero crossing in the mechanical interrupter to facilitate successful interruption by de-saturating the injection inductor.

The controllable inductor was investigated using experiments and simulations. In a first step, a scaled-down current injection circuit was built and tested. The obtained data was then compared with a

simulation model to evaluate its accuracy. Differences between measurement and simulation have been observed, which are attributed to inaccurate material parameters and simplifications in modelling (skin effect, hysteresis of material not modelled, geometry). However, currents and voltages are still in a comparable range and the general trends of simulation and experiment match.

In a second step, to judge the feasibility of using controllable inductors in HVDC systems, a second simulation study was conducted. This study suggests that controllable inductors for this purpose require high, but attainable, control current levels. Core volume and insulation requirements are reasonable. While the economic advantage of such a design is difficult to estimate, the technical advantages motivate further research. This includes implementation of more complex models as well as a determination of the optimum core material. Furthermore, an algorithm to predict and circuitry to adjust the control current based on a measurement of the fault current has to be developed. A suitable design also could reduce stresses at interruption for the MI sufficiently to enable the use of a gas interrupter instead of a series connection of vacuum interrupters. This would further reduce complexity and enable a more economic design.

Acknowledgment

The work presented in this paper was supported by the Swiss Federal Commission for Innovation and Technology within the SCCER-FURIES.

7 References

- Bordignon, P., Bathurst, G. 'Delivery of the Nan'ao multi-terminal VSC-HVDC system'. In: 11th IET International Conference on AC and DC Power Transmission. (, 2015).
- Wandi, Z., Wei, X., Zhang, S., Tang, G., He, Z., Zheng, J., et al.: 'Development and test of a 200kV full-bridge based hybrid HVDC breaker', *EPE-ECCE Europe*, 2015, pp. 1–7
- Pang, H., Wei, X. 'Research on Key Technology and Equipment for Zhangbei 500kV DC Grid'. In: 2018 International Power Electronics Conference. (IEEE, 2018, pp. 2343–2351
- Franck, C.M., Smeets, R., members A3/B4..34. 'Technical Requirements and Specifications of State-of-the-Art HVDC Switching Equipment'. (Cigré Technical Brochure 683, 2017.
- Greenwood, A., Lee, T.: 'Theory and Application of the Commutation Principle for HVDC Circuit Breakers', *IEEE Trans Power App Sys*, 1972, **PAS-91**, (4), pp. 1570–1574
- Callavik, M., Blomberg, A.: 'The Hybrid HVDC Breaker an innovation breakthrough enabling reliable HVDC grids', *ABB Grid Systems, Technical Paper*, 2012, **361**, pp. 143–152
- Grieshaber, W., Dupraz, J., Penache, D.L., Violleau, L.: 'Development and test of a 120 kv direct current circuit breaker', *Proc CIGRE Session, Paris*, 2014, pp. 1–11
- Sima, W., Fu, Z., Yang, M., Yuan, T., Sun, P., Han, X., et al.: 'A Novel Active Mechanical HVDC Breaker With Consecutive Interruption Capability for Fault Clearances in MMC-HVDC Systems', *IEEE Transactions on Industrial Electronics*, 2019, **66**, (9), pp. 6979–6989
- Arimatsu, K., Yoshioka, Y., Tokuyama, S., Kato, Y., Hirata, K.: 'Development and Interrupting Tests on 250KV 8KA HVDC Circuit Breaker', *IEEE Transactions on Power Apparatus and Systems*, 1985, **PAS-104**, (9), pp. 2452–2459
- Lee, A., Slade, P., Yoon, K., Porter, J., Vithayathil, J.: 'The Development of a HVDC SF6 Breaker', *IEEE Transactions on Power Apparatus and Systems*, 1985, **PAS-104**, (10), pp. 2721–2729
- Greenwood, A., Barkan, P., Kracht, W.C.: 'HVDC Vacuum Circuit Breakers', *IEEE Transactions on Power Apparatus and Systems*, 1972, **PAS-91**, (4), pp. 1575–1588
- Damsky, B.L., Imam, I., Premerlani, W. 'A New HVDC Circuit Breaker System Design For +- 400 kV'. In: IEEE/PES Transmission and Distribution Conference and Exposition. (IEEE, 1979, pp. 230–236
- Tahata, K., El Oukaili, S., Kamei, K., Yoshida, D., Kono, Y., Yamamoto, R., et al. 'HVDC circuit breakers for HVDC grid applications'. In: IET Conference on AC and DC Power Transmission. (Birmingham, UK, 2015, pp. 1–9
- Yanabu, S., Tamagawa, T., Irokawa, S., Horiuchi, T., Tomimuro, S.: 'Development of HVDC Circuit Breaker and its Interrupting Test', *IEEE Transactions on Power Apparatus and Systems*, 1982, **PAS-101**, (7), pp. 1958–1965
- Senda, T., Tamagawa, T., Higuchi, K., Horiuchi, T., Yanabu, S.: 'Development of HVDC Circuit Breaker Based on Hybrid Interruption Scheme', *IEEE Transactions on Power Apparatus and Systems*, 1984, **PAS-103**, (3), pp. 545–552
- Belda, N.A., Plet, C.A., Smeets, R.P.P.: 'Full-Power Test of HVDC Circuit-Breakers with AC Short-Circuit Generators Operated at Low Power Frequency', 2018, **8977**, (c), pp. 1–11
- Jovicic, D., Tang, G., Pang, H.: 'Adopting Circuit Breakers for High-Voltage dc Networks: Appropriating the Vast Advantages of dc Transmission Grids', *IEEE Power and Energy Magazine*, 2019, **17**, (3), pp. 82–93

- 18 Leishi, X., Chao, S., Qifu, L. 'Research on short-circuit test and simulation of csg first mechanical hvdc circuit breaker in vsc-hvdc'. In: International Conference on Power System Technology. (IEEE, 2018. pp. 2764–2769
- 19 Schultz, T., Hammerich, B., Bort, L., Franck, C.M.: 'Improving interruption performance of mechanical circuit breakers by controlling pre-current-zero wave shape', *High Voltage*, 2019,
- 20 Schultz, T., Herzog, P., Franck, C.M.: 'Interruption Limits of Mechanical Circuit Breakers and Circuit Upgrades for Current Injection in HVDC Circuit Breakers', *to be published*, 2019,
- 21 Schultz, T., Herzog, P., Franck, C.M. 'Current Injection Circuit Breakers for HVDC: Overview on Improved Injection Circuits'. In: accepted at: ICEPE-ST. (, 2019.
- 22 Lynn, G.E.: 'Self-saturating magnetic amplifiers'. (New York: McGraw-Hill, 1960)
- 23 McLyman, C.: 'Transformer and Inductor Design Handbook, Fourth Edition'. 4th ed. (CRC Press, 2011)
- 24 Alexanderson, E.F.W.: 'Transatlantic radio communication', *Proceedings of the American Institute of Electrical Engineers*, 1919, **38**, (10), pp. 1077–1093
- 25 Schultz, T., Franck, C.M. 'Interruption Capability Investigations of a Model Gas Circuit-Breaker for HVDC Switching Applications'. In: International Conference on Gas Discharges and their Applications. (, 2016. pp. 173–176